JACS
JOURNAL OF THE AMERICAN CHEMICAL SOCIETY

Article

pubs.acs.org/JACS

Electrochemical Synthesis of Mesoporous Pt–Au Binary Alloys with Tunable Compositions for Enhancement of Electrochemical Performance

Yusuke Yamauchi,*[,†,‡,§,∥] Akihisa Tonegawa,[§] Masaki Komatsu,[§] Hongjing Wang,[†,§] Liang Wang,[†] Yoshihiro Nemoto,[†] Norihiro Suzuki,[†] and Kazuyuki Kuroda*[,§,∥]

[†]World Premier International (WPI) Research Center for Materials Nanoarchitectonics (MANA), National Institute for Materials Science (NIMS), 1-1 Namiki, Tsukuba, Ibaraki 305-0044, Japan

[‡]PRESTO, Japan Science and Technology Agency (JST), 4-1-8 Honcho, Kawaguchi, Saitama 332-0012, Japan

[§]Faculty of Science and Engineering, Waseda University, 3-4-1 Ohkubo, Shinjuku, Tokyo 169-8555, Japan

[∥]Kagami Memorial Laboratory for Materials Science and Technology, Waseda University, 2-8-26 Nishi-Waseda, Shinjuku, Tokyo 169-0051, Japan

Supporting Information

ABSTRACT: Mesoporous Pt–Au binary alloys were electrochemically synthesized from lyotropic liquid crystals (LLCs) containing corresponding metal species. Two-dimensional exagonally ordered LLC templates were prepared on conductive substrates from diluted surfactant solutions including water, a nonionic surfactant, ethanol, and metal species by drop-coating. Electrochemical synthesis using such LLC templates enabled the preparation of ordered mesoporous Pt–Au binary alloys without phase segregation. The framework composition in the mesoporous Pt–Au alloy was controlled simply by changing the compositional ratios in the precursor solution. Mesoporous Pt–Au alloys with low Au content exhibited well-ordered 2D hexagonal mesostructures, reflecting those of the original templates. With increasing Au content, however, the mesostructural order gradually decreased, thereby reducing the electrochemically active surface area. Wide-angle X-ray diffraction profiles, X-ray photoelectron spectra, and elemental mapping showed that both Pt and Au were atomically distributed in the frameworks. The electrochemical stability of mesoporous Pt–Au alloys toward methanol oxidation was highly improved relative to that of nonporous Pt and mesoporous Pt films, suggesting that mesoporous Pt–Au alloy films are potentially applicable as electrocatalysts for direct methanol fuel cells. Also, mesoporous Pt–Au alloy electrodes showed a highly sensitive amperometric response for glucose molecules, which will be useful in next-generation enzyme-free glucose sensors.

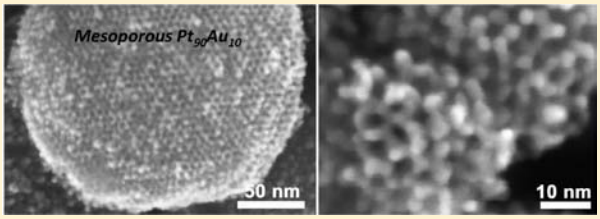

1. INTRODUCTION

Noble metals such as Pt and Au are highly resistant to corrosion or oxidation, unlike most base metals, and they are known as the most chemically stable metals. Recently, nanostructured noble metals have been extensively explored because of their unique physical and chemical properties, which are different from those of the metals in bulk.[1,2] In particular, Pt-based nanomaterials (e.g., nanoparticles, nanotubes, nanofibers, and nanoporous materials) have been widely researched and are expected to be used in exciting technological applications, including fuel cells, hydrogenation, sensors, and catalysts.[3−7] Although Au previously was known to be catalytically less active than other metals, the discovery of Au-based catalysts with extraordinarily high catalytic activity for a variety of reactions, including low-temperature CO oxidation, has driven recent interest in Au chemistry and Au-based nanomaterials.[8−10]

Recent reports have demonstrated that Pt–Au alloy nanoparticles have unique effects on catalysis, which is of fundamental interest and importance for further enhanced functionalities.[11−16] The Pt–Au bimetallic system is very interesting because it has more unusual catalytic properties than pure Au and pure Pt. The Pt–Au alloy surface shows outstanding electrocatalytic performance for methanol oxidation reactions in fuel cells because the presence of Au suppresses the adsorption of poisoning species, such as CO.[17] However, in general, Pt and Au are difficult to form in a homogeneous binary alloy state. Therefore, phase segregation has often been reported.[18−21] The creation of a binary Pt–Au alloy is a worthwhile challenge. Although many efforts have been made to prepare bimetallic Pt–Au nanomaterials under various synthetic conditions, their processes are still complicated because of the different reduction kinetics of Au and Pt ions.

Received: September 26, 2011
Published: February 21, 2012

   dx.doi.org/10.1021/ja209044g | J. Am. Chem. Soc. 2012, 134, 5100–5109

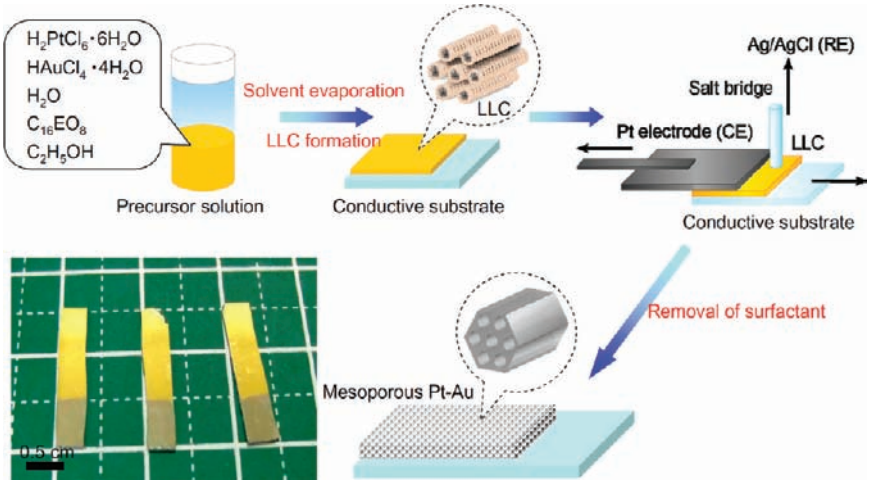

Figure 1. Illustration of the experimental procedure for preparation of mesoporous Pt–Au alloy films by electrochemical deposition. The photographs show mesoporous Pt–Au films deposited on Au-coated Si substrates.

In this report, we propose the introduction of mesoporous structures in Pt–Au binary alloy systems using as templates lyotropic liquid crystals (LLCs) containing highly concentrated surfactants. Metallic mesoporous structures can provide high surface areas and large pore volumes as well as high electroconductivity, which are important factors for electrochemical applications.[22] Since the first report of mesoporous Pt by Attard et al. in 1997,[23] various kinds of mesoporous metals with different compositions have been reported.[24−36] However, mesoporous alloys containing Au have never been reported because of difficulty of synthesizing them. The general synthesis involves the formation of the LLC template followed by the reduction of metal ions in the presence of the LLC. LLCs consisting of highly concentrated surfactants (normally >40 wt %)[37−40] are generally prepared by manually mixing ternary components (including surfactants, water, and metal species). This process is repeated until a homogeneous mixture is obtained. As is generally known, Au ions are easily deposited under sunlight or at high temperature; thus, preferential Au deposition is unavoidable (see the example in Figure S1 in the Supporting Information). Here we successfully prepared mesoporous Pt–Au alloys by utilizing LLC films spontaneously formed from a diluted surfactant solution through solvent evaporation. The LLC helps the Au and Pt ions to be uniformly distributed, as the ions interact effectively with the ethylene oxide groups of the surfactant. Therefore, both Pt and Au species in the presence of the LLC are thought to be uniformly reduced despite the different deposition potentials for the Au and Pt ions, thereby enabling the preparation of a perfect Pt–Au alloy state. Wide-angle X-ray diffraction (XRD), X-ray photoelectron spectroscopy (XPS), and elemental mapping clearly proved that both Pt and Au were atomically distributed in the frameworks without phase segregation. The electrochemical stability of the mesoporous Pt–Au alloys toward methanol oxidation was highly improved relative to that of nonporous Pt and mesoporous Pt films. The mesoporous Pt–Au alloy films showed high potential for use as an electrocatalyst in direct methanol fuel cells. Also, the mesoporous Pt–Au alloy electrodes showed a highly sensitive amperometric response for glucose molecules, which will be useful for enzyme-free glucose sensors in the future. Through the potential electrochemical applications, we have clearly demonstrated several benefits provided by alloying Pt with Au, which we believe to be an important technology for securing high functionality.

2. EXPERIMENTAL PROCEDURES

2.1. Materials. The nonionic surfactant octaethylene glycol monohexadecyl ether, $C_{16}H_{33}(OCH_2CH_2)_8OH$ ($C_{16}EO_8$), was used to form the LLCs. Hydrogen hexachloroplatinate(IV) hydrate ($H_2PtCl_6 \cdot 6H_2O$ purity >98.5%, Kanto Kagaku Co.) and hydrogen tetrachloroaurate(III) tetrahydrate ($HAuCl_4 \cdot 4H_2O$ purity >99.0%, Kanto Kagaku Co.) were used as Pt and Au sources, respectively. Ethanol (H_2O content <0.005%, Wako Chemical Co.) was used both for dilution of the precursor solution and removal of surfactants. Indium tin oxide (ITO) or Au-coated silicon substrates were used as working electrodes. For the preparation of Au-coated silicon substrates, Ti and Au layers were uniformly coated onto the Si substrate by vacuum deposition. A 100 nm gold layer was then deposited in an ULVAC CRTM-6000 electron-beam evaporation chamber preceded by a 20 nm titanium layer. The titanium layer promotes adhesion between the gold layer and the silicon dioxide surface.

2.2. Preparation of Mesoporous Pt–Au Films. The preparation process is systematically displayed in Figure 1. First, two-dimensional (2D) hexagonally ordered LLC templates were prepared on conductive substrates from diluted surfactant solutions including water, nonionic surfactant, ethanol, and metal species by drop-coating.[41−44] $H_2PtCl_6 \cdot 6H_2O$ and $HAuCl_4 \cdot 4H_2O$ were dissolved in distilled water in gradually varying $Au^{3+}/(Pt^{4+}+Au^{3+})$ mole ratios. The total concentration of Pt and Au species was maintained at 1.6 M. Next, the nonionic surfactant $C_{16}EO_8$ was added to the solutions. The concentration of the surfactant relative to water was adjusted to 55 wt %. Ethanol was added to the solution as a volatile solvent. The ethanol to surfactant ratio was adjusted to 85 wt %. The precursor solution was stirred for 40 min at room temperature and became a homogeneous solution with low viscosity (see Figure 2). The precursor was dip-coated onto a substrate and dried at 25 °C for 1 h. After the volatile solvent was completely evaporated, the LLC film including both Pt and Au species was formed over the entire substrate. Electrochemical depositions were then carried out for 30 s at room temperature at a constant potential (−0.04 V vs Ag/AgCl) using a potentiostat/galvanostat (model HA-151, Hokuto Denko Corp.). The Pt substrate used as the counter electrode was placed onto the LLC-modified substrate to sandwich the LLC. The Ag/AgCl electrode used as the reference electrode was connected to the LLC using a salt bridge (Figure 1). After the metal deposition, the deposits were washed with ethanol and water to remove surfactants and undeposited metal species.

dx.doi.org/10.1021/ja209044g | J. Am. Chem. Soc. 2012, 134, 5100−5109

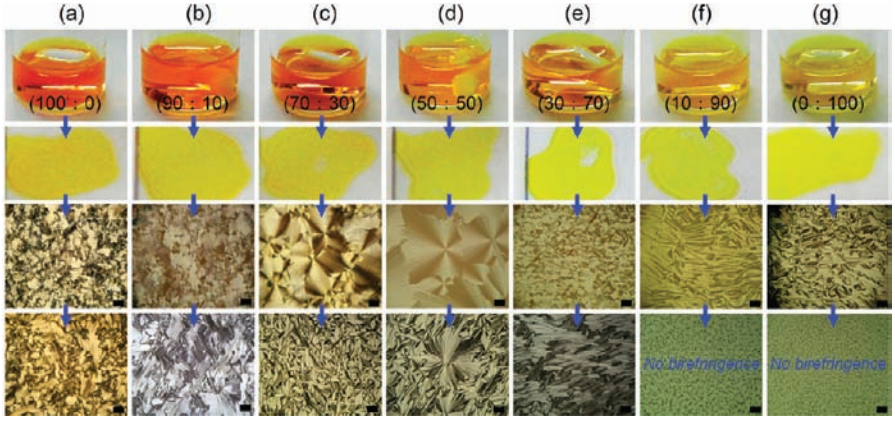

Figure 2. (top two lines) Photographs of the precursor solutions and the LLC films obtained after solvent evaporation. (bottom two lines) Polarized optical microscopy (POM) images of the LLC films. The last line shows POM images obtained after 30 min. The scale bar is 10 μm. The Pt^{4+}:Au^{3+} compositional ratios in the precursor solutions are noted in parentheses.

2.3. Characterizations. The liquid-crystalline state of the LLC films on glass substrates was confirmed by polarized optical microscopy (POM) using an Olympus BX-51 optical microscope under a crossed Nicol field; the images were recorded on a digital camera (Canon IXY DIGITAL 800 IS). The θ–2θ scanning profiles at the lower diffraction angles were measured using a Mac Science M03XHF22 diffractometer with Mn-filtered Fe Kα radiation (40 kV, 20 mA). The 2D XRD patterns were measured using Rigaku RINT RAPID diffraction system with Co radiation (40 kV, 20 mA). Scanning electron microscopy (SEM) images were obtained using Hitachi S-4800 and Hitachi S-5500 microscopes. Transmission electron microscopy (TEM) images were taken using a JEOL JEM-2010 microscope at an accelerating voltage of 200 kV. Energy-disersive spectroscopy (EDS) mapping was performed using a JEM-2100F microscope at an accelerating voltage of 200 kV.

2.4. Electrochemical Tests. All electrochemical measurements were done in a three-electrode system. The electrochemically active surface areas (ECSAs) of mesoporous Pt and Pt–Au alloy films were calculated from the reduction peaks of platinum oxide species and Au oxide species in cyclic voltammograms (CVs) obtained in an alkaline medium (0.1 M NaOH) at a scan rate of 20 mV s^{-1}. On the basis of the assumption that the charges associated with the reduction of the oxide species are 543 and 493 mC m^{-2} for Pt and Au surfaces, respectively, the ECSAs were theoretically calculated. Methanol electrocatalytic oxidation measurements were carried out in a 0.5 M H_2SO_4 solution containing 0.5 M methanol at a scan rate of 50 mV·s^{-1}. In the electrocatalytic investigations, the ECSAs were used to normalize the current. Before the above electrochemical measurements, nitrogen gas was used for purging (about 30 min) to remove dissolved O_2 from the electrolyte solutions. Glucose detection using mesoporous Pt and Pt–Au alloy films was also evaluated. A 0.1 M phosphate-buffered saline (PBS) solution containing 0.15 M NaCl was used. The concentration of the added glucose solution was 1 mM. The signals for the added glucose solution were measured by amperometric curves in a quiescent solution.

3. RESULTS AND DISCUSSION

Figure 2 shows POM images of LLC films including Pt and Au species. All of the LLC films showed clear birefringence. 2D XRD patterns (Figure S2 in the Supporting Information) showed three spots assigned to (10), (1$\bar{1}$), and (01) in 2D hexagonal symmetry. Low-angle XRD profiles also showed (10) and (20) peaks for the 2D hexagonal mesophases (Figure S3 in the Supporting Information). The absence of the (11) peak indicated that rodlike self-assemblies were formed with the (10) face aligned parallel to the substrate. The stability of the LLC films decreased with increasing amounts of Au (with Pt^{4+}:Au^{3+} = 10:90 and 0:100). Although the LLC films showed obvious textures at the initial stage, the textures completely disappeared within 30 min (Figure 2). The 2D XRD patterns for these LLC films (not shown) also exhibited no spots, indicating the collapse of the initial 2D hexagonal mesophases.

In previous reports, Dag and co-workers investigated the conformation state of dissolved metal ions in various LLC systems.[45–48] There are two types of conformation of the dissolved metal ions: *direct* and *indirect* coordination with ethylene oxide groups of the surfactant. As an example of the former, the LLC system consisting of $[Co(H_2O)_6]X_2$ (X = NO^{3-}, Cl^-, ClO^-) and P65 [PEO_{25}–PPO_{30}–PEO_{25}; PEO = poly(ethylene oxide), PPO = poly(propylene oxide)] was reported.[46] At equilibrium, the Co^{2+} species were directly coordinated with the ethylene oxide groups of P65 without the formation of Co^{2+}–aqua complexes. Such a coordination state caused the formation of disordered LLC regions. In particular, a dry atmosphere accelerated the evaporation of the coordinated water molecules in the Co^{2+}–aqua complexes, leading to the collapse of the ordered LLC mesophases. On the other hand, in the other LLC systems, the dissolved metal ions are coordinated by water molecules to form metal–aqua complexes.[47,48] Hydrogen bonds between ethylene oxide groups of the surfactant and coordinated water molecules are formed, resulting in the stabilization of the metal aqua complexes in the LLC (i.e., the coordinated water molecules are not easily evaporated in the atmosphere). Consequently, the conformation state of the dissolved metal ions has a strong influence on the LLC stability.

In the present systems, the evaporation of the water molecules accelerated with increases in the amount of dissolved Au ions, leading to the collapse of the ordered 2D mesophases. On the basis of the results, it was speculated that the Au^{3+} ions derived from $HAuCl_4$ were favorably and directly coordinated with ethylene oxide groups, while the Pt^{4+} ions were coordinated by water molecules to form metal–aqua complexes whose coordinated water molecules were also coordinated with ethylene oxide groups by hydrogen bonds. As shown in Figure S3, the basal spacings of the (10) peaks were calculated to be 4.76 nm for Pt^{4+}:Au^{3+} = 100:0, 4.68 nm for Pt^{4+}:Au^{3+} = 94:6, 4.47 nm for Pt^{4+}:Au^{3+} = 80:20, and 4.35 nm for Pt^{4+}:Au^{3+} = 30:70. Thus, the basal spacings decreased as amount of dissolved Au^{3+} ions increased. Such a decrease means a decrease of the hydrophilic region, which is evidence of the

dx.doi.org/10.1021/ja209044g | J. Am. Chem. Soc. 2012, 134, 5100–5109

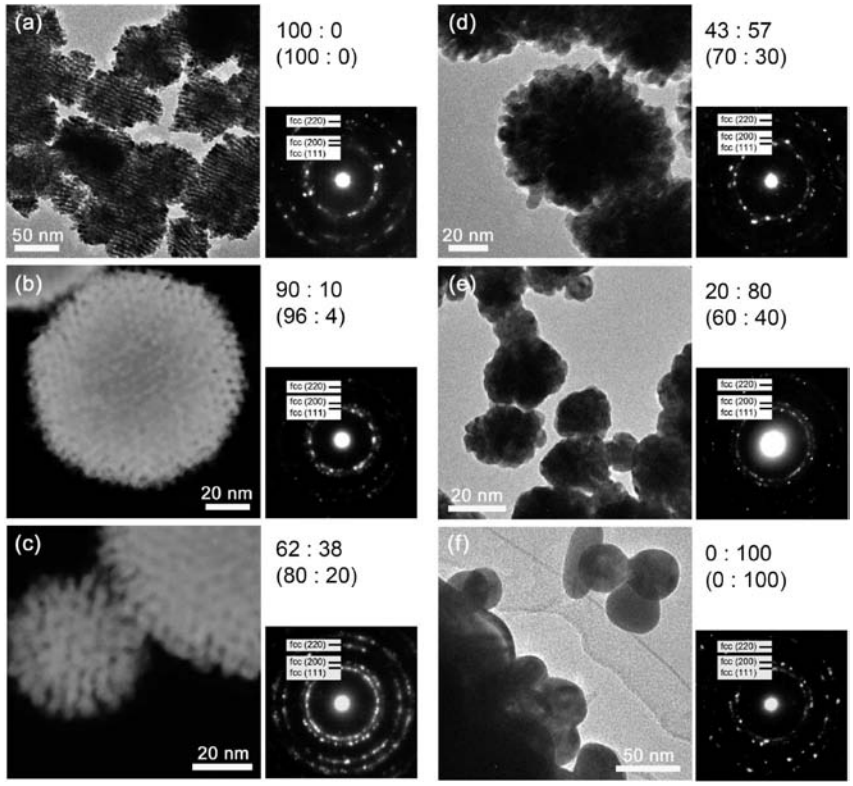

Figure 3. Bright-field and dark-field TEM images for the samples deposited from LLC films with different compositions. The insets show SAED patterns taken from an area of 40 000 nm^2 (200 nm × 200 nm). The product compositions (Pt:Au) are noted. The Pt^{4+}:Au^{3+} compositional ratios in the precursor solutions used are also noted in parentheses.

decrease of the coordinated water contents with the increase in the amount of Au^{3+} ions. Thus, in the case of the LLC with a high content of Au^{3+} ions, the coordinated water molecules quickly evaporated under the normal atmosphere, and the stability of the LLC was dramatically decreased. However, when the LLC films after the collapse of the ordered mesophases were placed under conditions of saturated humidity, the textures reappeared and were retained for more than 1 week. The appearance of ordered LLC mesophases was caused by the dissolution of a sufficient number of coordinated water molecules into the LLC under the saturated humidity.

LLC films with various compositional ratios were prepared on conductive ITO substrates. Mesoporous Pt–Au alloy particles with different compositions were then deposited. Their compositions, mesostructures, and atomic crystallinities were carefully characterized. TEM and SEM images showed that the deposits consisted of aggregated spherical particles (Figures 3 and 4). The particle size distribution was in the range from 50 to 500 nm. Figure 5 shows the relationship between the LLC composition and the product composition, which was estimated by inductively coupled plasma (ICP) analysis. The deposited alloys contained relatively Au-rich phases over the entire range of LLC compositions. The Au content in the products increased remarkably in the LLC composition range of $Au^{3+}/(Pt^{4+}+Au^{3+})$ = 0.0–0.4. The Au content in the products did not change so greatly when the LLC composition was above $Au^{3+}/(Pt^{4+}+Au^{3+})$ = 0.7. Because the reduction potential of $AuCl_4^-$/Au (+1.00 V vs SHE) is quite different from that of $PtCl_4^{2-}$/Pt (+0.76 V vs SHE), the Au species were preferentially reduced under our experimental conditions. In any case, the composition of the products could be varied by varying the LLC composition.

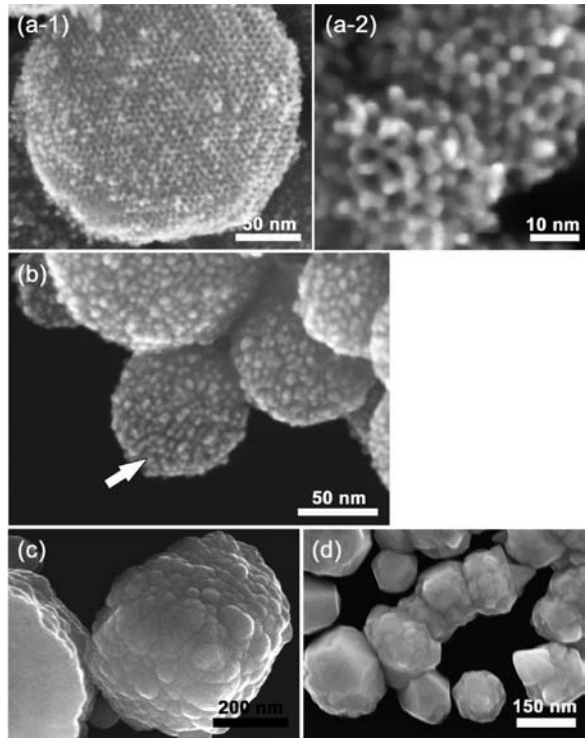

Figure 4. SEM images of the samples deposited from LLC films with different compositions: (a) mesoporous $Pt_{90}Au_{10}$ prepared from a film with $Au^{3+}/(Pt^{4+}+Au^{3+})$ = 0.04; (b) mesoporous $Pt_{62}Au_{38}$ prepared from a film with $Au^{3+}/(Pt^{4+}+Au^{3+})$ = 0.2; (c) $Pt_{20}Au_{80}$ deposit prepared from a film with $Au^{3+}/(Pt^{4+}+Au^{3+})$ = 0.4; (d) Au deposit prepared from a film with $Au^{3+}/(Pt^{4+}+Au^{3+})$ = 1.0.

dx.doi.org/10.1021/ja209044g | J. Am. Chem. Soc. 2012, 134, 5100–5109

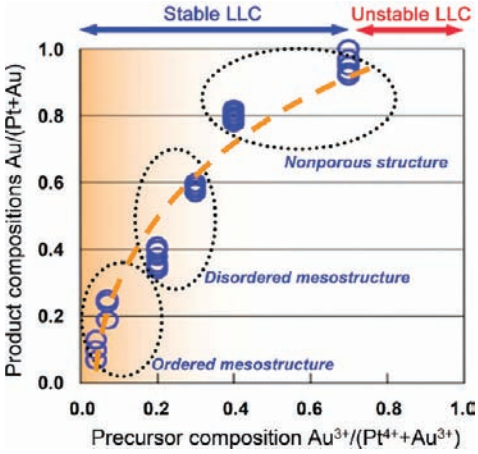

Figure 5. Relationship between the LLC composition and the product composition. The product composition was estimated by ICP analysis.

From the high-resolution SEM and TEM images, mesoporous Pt and Pt−Au alloys with low Au content (<10 atom %) possessed well-ordered 2D hexagonal mesoporous structures that were perfectly originated from the initial LLC structure (Figure 3a,b). From the highly magnified SEM images, honeycomb arrangements of uniform mesopores were directly observed on the external surface of the particle (Figure 4a-1). Analysis of the image yielded a pore diameter of ∼3.0 nm and a thickness of the pore wall of ∼3.0 nm, and the pore−pore distance was found to be 6−7 nm. The SEM image in Figure 4a-2 shows that the size of the Pt nanoparticles forming the framework varied slightly and correspondingly that the mesopores were also variable. Therefore, the periodicity of the mesostructures was slightly different at each location. The mesopore walls were composed of connected nanoparticles with an average size of ∼3 nm (Figure 4a-2). We observed a similar phenomenon for mesoporous Pt particles prepared by chemical reduction in our previous work, in which we explained the formation of connected nanoparticles by the mechanism of nanoscale metal deposition in the presence of the LLC.[36] With an increase in the amount of dissolved Au^{3+} ions [$Au^{3+}/(Pt^{4+}+Au^{3+})$ = 0.2−0.4], the ordered mesoporous structure became distorted. Mesoporous $Pt_{62}Au_{38}$ alloys [prepared from films with $Au^{3+}/(Pt^{4+}+Au^{3+})$ = 0.2] showed a disordered structure (Figure 3c), although ordered straight mesochannels were partially observable (as indicated by the arrow in Figure 4b). Mesoporous $Pt_{43}Au_{57}$ [prepared from films with $Au^{3+}/(Pt^{4+}+Au^{3+})$ = 0.3] possessed no obvious ordered mesostructure (Figure 3d). When the amount of dissolved Au^{3+} ions was further increased [$Au^{3+}/(Pt^{4+}+Au^{3+})$ = 0.4−1.0], only bulky deposits without mesoporosity were formed (Figures 3e,f and 4c,d). Especially when the Au species were reduced from LLC, the surface of the deposited particle was very smooth compared with those of others, and the particles showed a single-crystalline nature (Figure S4 in the Supporting Information). This observation indicates that unlike the Pt species, the Au species tend to grow rapidly in the LLC mesophases with retention of the atomic crystallinity, which may destroy the ordered LLC mesophase. Therefore, the ordered mesostructure became disordered and bulky with increasing Au content in the products.

For all the samples, the selected-area electron diffraction (SAED) patterns taken from 40 000 nm^2 (200 nm × 200 nm) regions (Figure 3 insets) showed ring patterns assignable to a face-centered cubic (fcc) structure. No phase separations for Pt and Au were observed, indicating the formation of a single phase (fcc structure) as a substitutional solid solution in which Pt atoms were partially replaced by Au atoms (wide-angle XRD profiles are given in a later section). To confirm the alloy state further, nanoscale EDS elemental mapping was carried out by TEM (Figure 6). The dark-field (DF) scanning TEM (STEM)

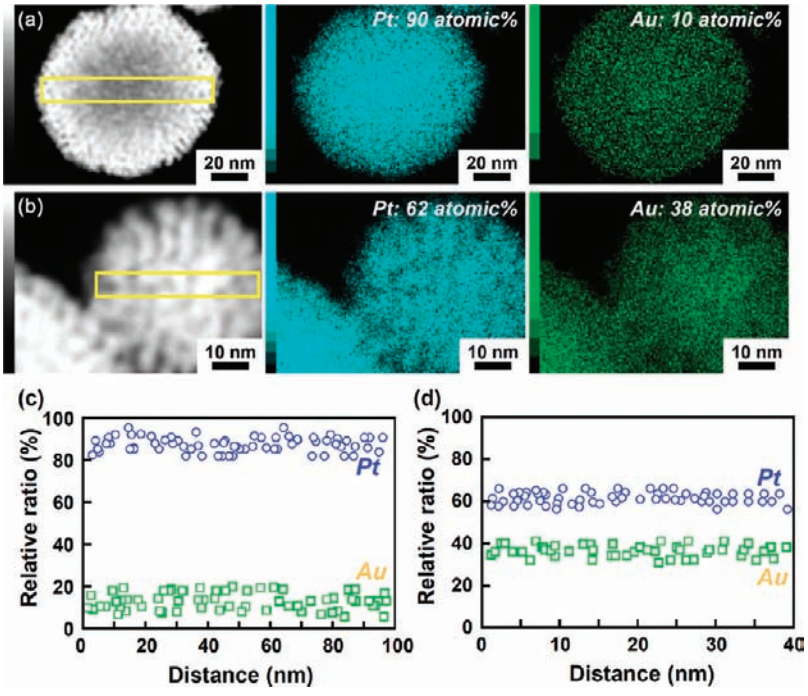

Figure 6. (a, b) Elemental mappings for (a) mesoporous $Pt_{90}Au_{10}$ prepared from a film with $Au^{3+}/(Pt^{4+}+Au^{3+})$ = 0.04 and (b) mesoporous $Pt_{62}Au_{38}$ prepared from a film with $Au^{3+}/(Pt^{4+}+Au^{3+})$ = 0.2. (c, d) Cross-sectional compositional line profiles of the square areas in (a) and (b), respectively.

dx.doi.org/10.1021/ja209044g | J. Am. Chem. Soc. 2012, 134, 5100−5109

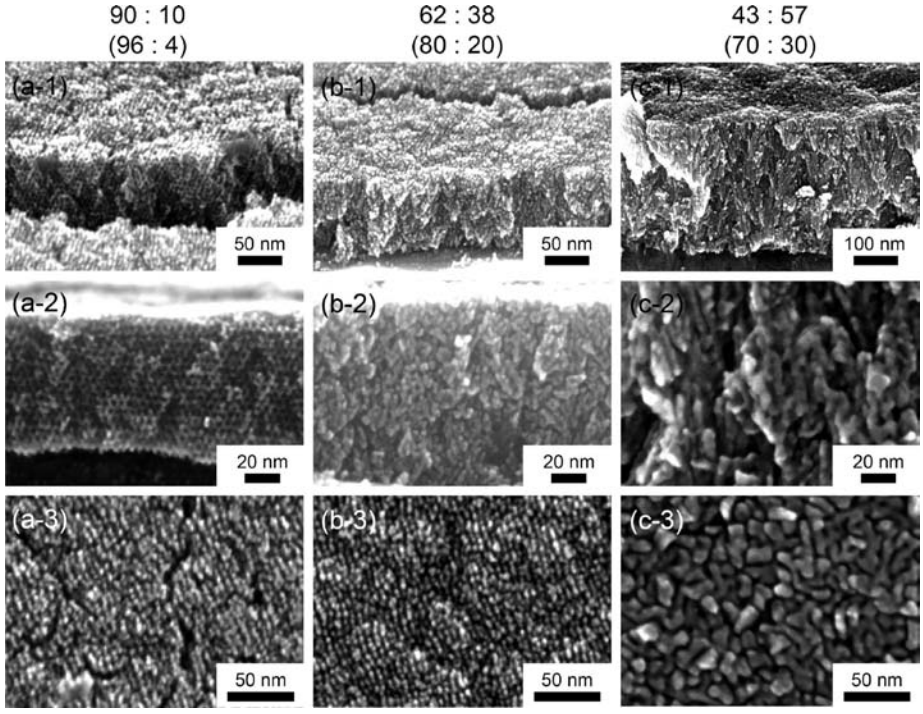

Figure 7. Highly magnified SEM images of the films deposited from LLCs with different compositions: (a-1, b-1, c-1) birds-eye views; (a-2, b-2, c-2) cross-sectional images; (a-3, b-3, c-3) top-surface images. The product compositions (Pt:Au) are noted at the top edge. The Pt^{4+}:Au^{3+} compositional ratios in the used precursor solutions are also given in parentheses.

image corresponds to the images of the EDS mappings of Pt and Au (Figure 6a,b). From the line-scanning profile across the particle, it was more clearly visualized that the Pt and Au atoms were well-dispersed without any phase separations on the nanometer scale (Figure 6c,d). The calculated atomic ratios of Pt and Au were in good agreement with those from the ICP analysis (Figure 5).

The powdery morphology shown in Figures 3, 4, and 6 is of limited relevance for electrochemical or sensor devices in which the mesoporous metals are required as thin films. Through the use of Au-coated silicon substrates, continuous mesoporous Pt–Au thin films with tunable compositions were prepared. As shown in Figure 7, the obtained films were crack-free and had a uniform thickness over the entire area. For the formation of such continuous films, the selection of the substrate composition is important.[49,50] When the Au and Pt ions are electrochemically reduced onto the Au surface of the substrate, the atomic arrangements of the deposited Pt and Au reflect those of the Au surface. This is because the Au layer on the substrate also has an fcc structure that is identical to that of the deposited Pt–Au alloys. Therefore, the nucleation of Pt and Au easily occurs. In the present case, many Pt and Au nuclei were homogeneously generated on the Au-coated substrate in the initial stage of the deposition. Pt and Au then uniformly grew from the initial Pt nuclei. Thus, Pt and Au could be continuously deposited over the entire area of the Au-coated substrate. In contrast, when ITO substrates were used instead of Au-coated substrates (as shown in the above section), granular particles were deposited (Figure 3). The lattice parameters of the ITO surface are completely different from those of Pt. Because of the large mismatch of the parameters, the number of Pt nuclei generated in the initial stage is not sufficient for the formation of a continuous film.

Wide-angle XRD patterns for mesoporous Pt and Pt–Au alloy films are shown in Figure S5a in the Supporting Information. Two peaks derived from the deposited samples were observed, which can be assigned as the (111) and (200) peaks of the fcc crystal structure. Compared with the Pt alone (mesoporous Pt), the (111) peaks gradually shifted to a lower 2θ angle with increasing Au content. These peaks for mesoporous Pt–Au alloy films were observed between the peaks of Au and Pt as a single peak, indicating that the deposited Pt–Au was formed as a single-phase alloy. From the wide-angle XRD patterns, the d spacings of the (200) peaks for the corresponding alloys with different compositions were calculated. Figure S5b shows the relationship between the d spacing and the Au content in the deposited films. The d spacing increased linearly with increasing relative Au content, following Vegard's law. These results proved that the deposited Pt–Au was indeed an alloy phase rather than a mixture of monometallic or core–shell particles.[19,20]

From the cross-sectional elemental mapping of the mesoporous Pt–Au alloy film, both Pt and Au atoms were macroscopically dispersed over the entire area (Figure S6 in the Supporting Information). XPS spectra of the Pt 4f region for mesoporous Pt and representative Pt–Au samples are shown in Figure S7 in the Supporting Information. The intensities of the Pt peaks gradually decreased with increasing Au content in the film. The satellite peaks derived from the Au layers on the substrates overlapped with the Pt peaks. The peaks in the Pt region could be deconvoluted into different components of Pt $4f_{5/2}$, Pt $4f_{7/2}$, Pt–O $4f_{5/2}$, and Pt–O $4f_{7/2}$. It is noteworthy that the binding energies in the Pt region were negatively shifted with increasing Au content. As seen in the enlarged figure (Figure S7b), the two binding energies of Pt $4f_{5/2}$ and Pt–O $4f_{5/2}$ clearly shifted in a negative direction with increasing the Au content. The same situation has been observed in previous

dx.doi.org/10.1021/ja209044g | J. Am. Chem. Soc. 2012, 134, 5100–5109

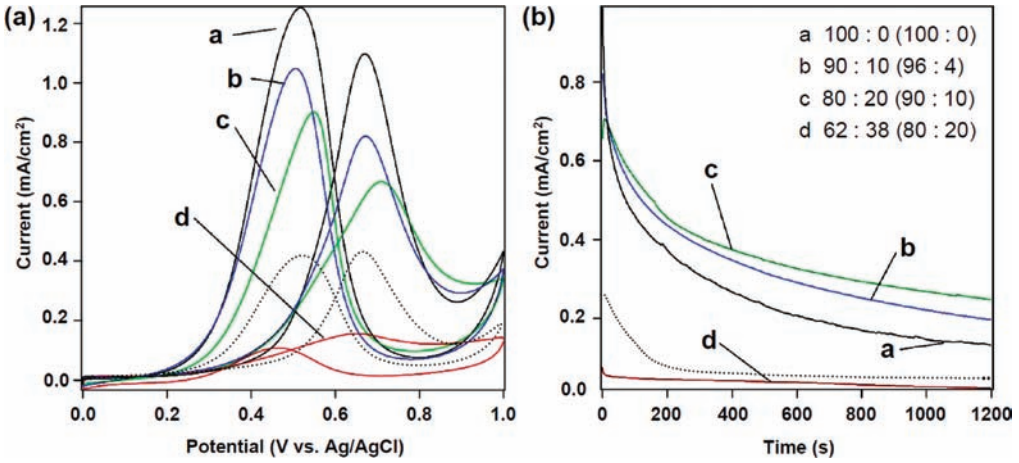

Figure 8. (a) CVs and (b) chronoamperometric curves at 0.6 V measured in 0.5 M H_2SO_4 containing 0.5 M methanol. The currents were normalized to the ECSAs obtained from CV curves in 0.1 M NaOH solution. The product compositions (Pt:Au) are noted, and the Pt^{4+}:Au^{3+} compositional ratios in the precursor solutions are also given in parentheses. As a reference, a bulk Pt film (dotted line) is compared with the other samples. The bulk Pt film was prepared by electrochemical deposition at a constant potential (−0.04 V vs Ag/AgCl). The film thicknesses for all of the samples were ∼100 nm.

reports on Pt-based alloys.[51,52] The negative shift observed here can be explained by the change of the Pt electronic structure in the alloy system. The Fermi level of Pt is higher than that of Au. Upon the addition of Au, a transfer of d-electron density from Pt to Au is observed, which effectively lowers the Fermi level of Pt.[51,52] This transfer could be observed from the binding energy of the f electrons, as shown in Figure S7. The gradual negative shift in the binding energy is important evidence that both Au and Pt are atomically mixed without phase separation.

Consequently, the use of the LLC as the template allowed us to prepare *perfect* Pt−Au binary alloys with mesoporous structures. Our previous works show the formation of Au@Pt core−shell nanoparticles consisting of a Au core and a nanostructured Pt shell when Au and Pt ions are reduced in the presence of low-concentration aqueous surfactant solution.[19,20] In that case, the Au ions were first reduced by a reducing agent to form the Au cores. After the consumption of the Au ions, the nanostructured Pt shells subsequently started to grow on the Au cores. In the low-concentration aqueous surfactant solution, Au and Pt ions could both diffuse freely. Therefore, such a phase separation (Au core and Pt shell) was caused by the different deposition potentials for the two types of ion, which is in contrast to the present study. In the LLCs with 2D hexagonally ordered mesophases (Figure 2), the rodlike self-assemblies are periodically arranged, and the hydrophilic domain with ethylene oxide groups is present among the rodlike self-assemblies. The dissolved Au and Pt ions are uniformly distributed over the entire LLC and effectively interact with the ethylene oxide groups of the surfactant tails, as described above. Upon application of electrochemical deposition, the metal deposition occurs inside the hydrophilic domains among the rods. Unlike the low-concentration surfactant system,[19,20] such a physically confined area for the metal deposition does not allow the metal ions to diffuse rapidly, so the metal deposition is thought to be unaffected by the different deposition potentials of the Au and Pt ions. Thus, the presence of the LLC can prevent the phase separation, thereby making possible the preparation of a perfect Pt−Au alloy state.

The ECSAs for mesoporous Pt and mesoporous Pt−Au films were calculated by using cyclic voltammetry in an alkaline medium (0.1 M NaOH). As shown in Figure S8 in the Supporting Information, the red-colored peak area is associated with the reduction of platinum oxide species, while the blue-colored peak area is associated with the reduction of gold oxide species. On the basis of the assumption that the charges associated with the reduction of oxide species are 543 and 493 mC cm^{-2} for Pt and Au surfaces, respectively, the ECSAs in the films were theoretically calculated from the observed charges shown in Figure S8.[53,54] The volume-normalized ECSAs were 433 m^2 cm^{-3} for mesoporous Pt, 213 m^2 cm^{-3} for mesoporous $Pt_{90}Au_{10}$ prepared from an LLC with $Au^{3+}/(Pt^{4+}+Au^{3+})$ = 0.04, and 185 m^2 cm^{-3} for mesoporous $Pt_{80}Au_{20}$ prepared from an LLC with $Au^{3+}/(Pt^{4+}+Au^{3+})$ = 0.1. These values are comparable to those of 2D hexagonally ordered mesoporous Pt films directly prepared from LLCs with $C_{16}EO_8$[26] and cage-type mesoporous Pt films prepared with a diblock copolymer.[49] However, the ECSAs decreased with increasing Au content because of the collapse of the mesostructural ordering (as shown in Figure 7). The volume-normalized ECSA of mesoporous $Pt_{62}Au_{38}$ [prepared at $Au^{3+}/(Pt^{4+}+Au^{3+})$ = 0.2] was 40.1 m^2 cm^{-3}. To investigate the thermal stability, mesoporous Pt and Pt−Au films were annealed at various temperatures for 3 h (Figure S9 in the Supporting Information). Even after the thermal treatments, the CV shapes for the two films did not change at all. No loss of specific surface areas was observed, indicating good thermal stability of the mesoporous films.

To investigate their potential use as catalytic electrodes, the methanol electrochemical oxidation reaction was examined. Figure 8 shows the electrocatalytic performances recorded in an aqueous solution containing methanol. All of the samples showed the two visible anodic peaks occurring on the positive and negative sweeps, which are typical features of the methanol oxidation process. In comparison with a nonporous Pt film without mesopores (as shown by the dotted line in Figure 8a), mesoporous Pt, $Pt_{90}Au_{10}$, and $Pt_{80}Au_{20}$ films showed a remarkably large current for the electrocatalytic oxidation of methanol. These specific activities of mesoporous films were found to be far larger than that of the nonporous Pt film. Three-dimensionally connected mesopores are known to make the entire surface readily accessible to reactants. Such porous

dx.doi.org/10.1021/ja209044g | J. Am. Chem. Soc. 2012, 134, 5100−5109

materials have little diffusion resistance for reactants such as methanol that have a mean free path shorter than the pore radius. However, increasing the Au content in the Pt−Au alloy led to a serious decrease in the methanol oxidation activity (Figure 8a, trace d) due to the insufficiency of active Pt atoms.[52] As a further demonstration of the durability of their catalytic performances, long-term oxidation of methanol was performed at a constant voltage of 0.6 V vs Ag/AgCl (Figure 8b). Both nonporous and mesoporous Pt electrodes suffered from serious deactivation, most likely due to poisoning. It is well-known that partially dehydrogenated intermediates act as poisons in the electro-oxidation of methanol.[55−57] In contrast, the mesoporous $Pt_{90}Au_{10}$ and $Pt_{80}Au_{20}$ films demonstrated a relatively higher current density for a long time. This result indicates that the presence of Au can remove such intermediates by oxidation,[15] showing sufficiently high durability of the catalytic performance of mesoporous Pt−Au alloy films. Even in comparison with other dendritic Pt nanoparticles and commercial Pt black powders,[58] our mesoporous Pt−Au alloy films can maintain very high catalytic performance for a long time.

As another practical application, mesoporous Pt−Au alloys can be potentially used for enzyme-free amperometric glucose sensing (Figure S10 in the Supporting Information). Currently, detection of the glucose concentration in human blood is particularly important for patients with diabetes mellitus. Although several different types of systems have been developed to determine the glucose level in blood, here we have demonstrated electrochemical amperometric detection of glucose molecules. Mesoporous Pt−Au alloy films with various compositions were compared with mesoporous Pt and bulk Pt films. The Figure S10b inset shows a linear-sweep voltammogram for a mesoporous $Pt_{80}Au_{20}$ alloy film at a potential scan rate of 10 mV s^{-1} in 0.1 M PBS (pH 7.4) containing 10 mM glucose. Two oxidation peaks occurring at around −0.4 and 0.2 V vs Ag/AgCl were confirmed clearly. These two peaks were caused by the glucose oxidation reaction on the Pt−Au surface. As shown in Figure S10a, to detect the actual signals corresponding to the added glucose solution, an amperometric measurement was performed at 0.4 V vs Ag/AgCl, which was positive enough to oxidize the glucose molecules. The overall kinetics of glucose electrooxidation on the bulk Pt film was too sluggish to produce significant Faradaic currents (Figure S10a). A similar situation occurred in the previous works, in which the activity of the Pt surface was seriously decreased by adsorbed chloride ions.[59−61] Also, the intermediate compounds produced by the glucose oxidation often covered the Pt surface, thereby decreasing the active Pt surface area. As shown in Figure S10b, on the mesoporous Pt surface, the amperometric responses corresponding to the successive additions of glucose solution were observed clearly. Recent reports have demonstrated that nanostructured electrocatalysts with highly active surfaces (e.g., mesoporous Pt, Pt nanotubes, and macroporous Pt) can improve the sensitivity of amperometric responses, even in the presence of chloride ions.[62−64] Furthermore, we could drastically improve the sensitivity of amperometric responses by alloying Pt with Au (Figure S10). With increases in the amounts of added glucose solution, the mesoporous Pt−Au alloy surface responded very well with linear dependence (R = 0.99) (Figure S10b). Although some efforts to modify Pt surfaces by using other metals have been made, the reason for the enhancement of the sensitivity is still unclear.[65−73] The enhanced performance observed here is most likely derived from the alloying of Pt with Au, which favors accelerating the sluggish reaction of glucose oxidation and effectively prevents the surface poisoning caused by adsorbed intermediates and chloride ion.

5. CONCLUSION

Mesoporous Pt−Au binary alloys were electrochemically synthesized from lyotropic liquid crystals (LLCs) containing corresponding metal species. The framework composition of the mesoporous Pt−Au alloy could be controlled by changing the compositional ratio in the precursor solution. From the wide-angle XRD profiles, XPS spectra, and elemental mapping, it was proved that both Pt and Au were atomically distributed in the frameworks. Mesoporous Pt−Au alloys with low Au content exhibit well-ordered 2D hexagonal mesostructures reflecting the original templates. With increasing Au content, however, the mesostructural ordering gradually decreased, thereby reducing the surface area. The electrochemical stability of mesoporous Pt−Au alloys in a methanol oxidation reaction was greatly improved relative to that of nonporous Pt and mesoporous Pt films. The addition of Au is very critical to reduce poisoning of the Pt surface, indicating that our mesoporous Pt−Au alloy films are potentially applicable as new electrocatalysts for direct methanol fuel cells. Furthermore, our mesoporous Pt−Au alloy films exhibited a very sensitive amperometric response for glucose molecules. Highly sensitive enzyme-free amperometric glucose sensors are particularly important for testing concentrations of glucose in human blood. Through this work, we have clearly demonstrated the important roles of fine control over the framework composition. Screening electrochemical tests using various mesoporous alloys with different compositions are quite necessary to bring out new functions and solid-state properties, which will be important for the further development of mesoporous metal research.

■ ASSOCIATED CONTENT

Ⓢ Supporting Information

Supporting Figures S1−S10. This material is available free of charge via the Internet at http://pubs.acs.org.

■ AUTHOR INFORMATION

Corresponding Author

Yamauchi.Yusuke@nims.go.jp; kuroda@waseda.jp

Notes

The authors declare no competing financial interest.

■ REFERENCES

(1) (a) Kusada, K.; Yamauchi, M.; Kobayashi, H.; Kitagawa, H.; Kubota, Y. *J. Am. Chem. Soc.* **2010**, *132*, 15896−15898. (b) Yamauchi, M.; Kobayashi, H.; Kitagawa, H. *ChemPhysChem* **2009**, *10*, 2566−2576. (c) Kobayashi, H.; Yamauchi, M.; Kitagawa, H.; Kubota, Y.; Kato, K.; Masaki, T. *J. Am. Chem. Soc.* **2010**, *132*, 5576−5577.

(2) Gu, J.; Fan, W.; Shimojima, A.; Okubo, T. *J. Solid State Chem.* **2008**, *181*, 957−963.

(3) (a) Guo, S. J.; Dong, S. J.; Wang, E. K. *Chem.—Eur. J.* **2008**, *14*, 4689−4695. (b) Li, T.; Du, Y.; Wang, E. K. *Chem.—Asian J.* **2008**, *3*, 1942−1948. (c) Zhang, L. X.; Wang, L.; Guo, S. J.; Zhai, J. F.; Dong, S. J.; Wang, E. K. *Electrochem. Commun.* **2009**, *11*, 258−261. (d) Guo, S. J.; Wen, D.; Zhai, Y. M.; Dong, S. J.; Wang, E. K. *ACS Nano* **2010**, *4*, 3959−3968. (e) Guo, S. J.; Dong, S. J.; Wang, E. K. *J. Phys. Chem. C* **2010**, *114*, 4797−4802. (f) Guo, S. J.; Wang, E. K. *Acc. Chem. Res.* **2011**, *44*, 491−500.

(4) Paxton, W. F.; Baker, P. T.; Kline, T. R.; Wang, Y.; Mallouk, T. E.; Sen, A. *J. Am. Chem. Soc.* **2006**, *128*, 14881−14888.
(5) (a) Wu, Y.; Livneh, T.; Zhang, Y. X.; Cheng, G.; Wang, J.; Tang, J.; Moskovits, M.; Stucky, G. D. *Nano Lett.* **2004**, *4*, 2337−2342. (b) Choi, K. S.; McFarland, E. W.; Stucky, G. D. *Adv. Mater.* **2003**, *15*, 2018−2021.
(6) (a) Zhang, X.; Lu, W.; Dai, J.; Wang, H.; Zhao, D.; Webley, P. A. *Chem. Commun.* **2009**, 195−197. (b) Zhang, X.; Lu, W.; Dai, J.; Bourgeois, L.; Hao, N.; Wang, H.; Zhao, D.; Webley, P. A. *Angew. Chem.* **2010**, *122*, 10299−10303.
(7) (a) Warren, S.; Messina, L.; Slaughter, L.; Kamperman, M.; Zhou, Q.; Gruner, S.; DiSalvo, F.; Wiesner, U. *Science* **2008**, *320*, 1748−1752. (b) Arora, H.; Li, Z.; Sai, H.; Kamperman, M.; Warren, S. C.; Wiesner, U. *Macromol. Rapid Commun.* **2010**, *31*, 1960−1964.
(8) Lee, S.; Fan, C.; Wu, T.; Anderson, S. L. *J. Am. Chem. Soc.* **2004**, *126*, 5682−5683.
(9) Tang, W.; Lin, H. F.; Kleiman-Shwarsctein, A.; Stucky, G. D.; McFarland, E. W. *J. Phys. Chem. C* **2008**, *112*, 10515−10519.
(10) Stokes, R. J.; Macaskill, A.; Dougan, J. A.; Hargreaves, P. G.; Stanford, H. M.; Smith, W. E.; Faulds, K.; Graham, D. *Chem. Commun.* **2007**, 2811−2813.
(11) Wang, J.; Thomas, D. F.; Chen, A. *Chem. Commun.* **2008**, 5010−5012.
(12) Lang, H.; Maldonado, S.; Stevenson, K. J.; Chandler, B. D. *J. Am. Chem. Soc.* **2004**, *126*, 12949−12956.
(13) Xu, J.; Zhao, T.; Liang, Z.; Zhu, L. *Chem. Mater.* **2008**, *20*, 1688−1690.
(14) Chen, G.; Li, Y.; Wang, D.; Zheng, L.; You, G.; Zhong, C. J.; Yang, L.; Cai, F.; Cai, J.; Chen, B. H. *J. Power Sources* **2011**, *196*, 8323−8330.
(15) Park, E. K.; Lee, J. K.; Kim, Y. S.; Kim, G. P.; Baeck, S. H. *J. Phys. Chem. Solids* **2008**, *69*, 1284−1287.
(16) Park, J. B.; Conner, S. F.; Chen, D. A. *J. Phys. Chem. C* **2008**, *112*, 5490−5500.
(17) Luo, J.; Maye, M. M.; Petkov, V.; Kariuki, N. N.; Wang, L.; Njoki, P.; Mott, D.; Lin, Y.; Zhong, C. J. *Chem. Mater.* **2005**, *17*, 3086−3091.
(18) Hernández-Fernández, P.; Rojas, S.; Ocón, P.; Gómez de la Fuente, J. L.; San Fabián, J.; Sanza, J.; Penã, M. A.; García-García, F. J.; Terreros, P.; Fierro, J. L. G. *J. Phys. Chem. C* **2007**, *111*, 2913−2923.
(19) Ataee-Esfahani, H.; Wang, L.; Nemoto, Y.; Yamauchi, Y. *Chem. Mater.* **2010**, *22*, 6310−6318.
(20) Ataee-Esfahani, H.; Wang, L.; Yamauchi, Y. *Chem. Commun.* **2010**, *46*, 3684−3686.
(21) Wang, L.; Yamauchi, Y. *Chem. Mater.* **2011**, *23*, 2457−2465.
(22) Yamauchi, Y.; Kuroda, K. *Chem.—Asian J.* **2008**, *3*, 664−676.
(23) Attard, G. S.; Göltner, C. G.; Corker, J. M.; Henke, S.; Templer, R. H. *Angew. Chem., Int. Ed. Engl.* **1997**, *36*, 1315−1317.
(24) Attard, G. S.; Bartlett, P. N.; Coleman, N. R. B.; Elliott, J. M.; Owen, J. R.; Wang, J. H. *Science* **1997**, *278*, 838−840.
(25) Nelson, P. A.; Elliott, J. M.; Attard, G. S.; Owen, J. R. *Chem. Mater.* **2002**, *14*, 524−529.
(26) Elliott, J. M.; Attard, G. S.; Bartlett, P. N.; Coleman, N. R. B.; Merckel, D. A. S.; Owen, J. R. *Chem. Mater.* **1999**, *11*, 3602−3609.
(27) Attard, G. S.; Leclerc, S. A. A.; Maniguet, S.; Russell, A. E.; Nandhakumar, I.; Bartlett, P. N. *Chem. Mater.* **2001**, *13*, 1444−1446.
(28) Wang, C.; Chen, D.; Jiao, X. *Sci. Technol. Adv. Mater.* **2009**, *10*, No. 023001.
(29) Boo, H.; Park, S.; Ku, B.; Kim, Y.; Park, J. H.; Kim, H. C.; Chung, T. D. *J. Am. Chem. Soc.* **2004**, *126*, 4524−4525.
(30) Jiang, J.; Kucernak, A. *J. Electroanal. Chem.* **2002**, *520*, 64−70.
(31) Jiang, J.; Kucernak, A. *J. Electroanal. Chem.* **2002**, *533*, 153−165.
(32) Kucernak, A.; Jiang, J. *Chem. Eng. J.* **2003**, *93*, 81−90.
(33) Jiang, J. H.; Kucernak, A. *J. Electroanal. Chem.* **2003**, *543*, 187−199.
(34) Yamauchi, Y.; Komatsu, M.; Fuziwara, M.; Nemoto, Y.; Sato, K.; Yokoshima, T.; Sukegawa, H.; Inomata, K.; Kuroda, K. *Angew. Chem., Int. Ed.* **2009**, *48*, 7792−7797.
(35) Yamauchi, Y.; Yokoshima, T.; Momma, T.; Osaka, T.; Kuroda, K. *Chem. Lett.* **2004**, *33*, 1576−1577.
(36) Yamauchi, Y.; Momma, T.; Fuziwara, M.; Nair, S. S.; Ohsuna, T.; Terasaki, O.; Osaka, T.; Kuroda, K. *Chem. Mater.* **2005**, *17*, 6342−6348.
(37) Albayrak, C.; Özkan, N.; Dag, Ö. *Langmuir* **2011**, *27*, 870−873.
(38) Dag, Ö.; Samarskaya, O.; Tura, C.; Günay, A.; Çelik, Ö. *Langmuir* **2003**, *19*, 3671−3676.
(39) Dag, Ö.; Alayoğlu, S.; Uysal, İ. *J. Phys. Chem. B* **2004**, *108*, 8439−8446.
(40) Attard, G. S.; Bartlett, P. N.; Coleman, N. R. B.; Elliott, J. M.; Owen, J. R. *Langmuir* **1998**, *14*, 7340−7342.
(41) Yamauchi, Y.; Momma, T.; Osaka, T.; Kuroda, K. Jpn. Kokai Tokkyo Koho JP2006233272 A2 20060907, 2004.
(42) Yamauchi, Y.; Momma, T.; Kitoh, H.; Osaka, T.; Kuroda, K. *Electrochem. Commun.* **2005**, *7*, 1364−1370.
(43) Yamauchi, Y.; Kitoh, H.; Momma, T.; Osaka, T.; Kuroda, K. *Sci. Technol. Adv. Mater.* **2006**, *7*, 438−445.
(44) Yamauchi, Y.; Ohsuna, T.; Kuroda, K. *Chem. Mater.* **2007**, *19*, 1335−1342.
(45) Albayrak, C.; Soylu, A. M.; Dag, Ö. *Langmuir* **2008**, *24*, 10592−10595.
(46) Albayrak, C.; Gülten, G.; Dag, Ö. *Langmuir* **2007**, *23*, 855−860.
(47) Demirörs, A. F.; Eser, B. E.; Dag, Ö. *Langmuir* **2005**, *21*, 4156−4162.
(48) Çelik, Ö.; Dag, Ö. *Angew. Chem., Int. Ed.* **2001**, *40*, 3799−3803.
(49) Takai, A.; Yamauchi, Y.; Kuroda, K. *J. Am. Chem. Soc.* **2010**, *132*, 208−214.
(50) Yamauchi, Y.; Sugiyama, A.; Morimoto, R.; Takai, A.; Kuroda, K. *Angew. Chem., Int. Ed.* **2008**, *47*, 5371−5373.
(51) Aricò, A. S.; Shukla, A. K.; Kim, H.; Park, S.; Min, M.; Antonucci, V. *Appl. Surf. Sci.* **2001**, *172*, 33−40.
(52) Tang, W.; Jayaraman, S.; Jaramillo, T. F.; Stucky, G. D.; McFarland, W. W. *J. Phys. Chem. C* **2009**, *113*, 5014−5024.
(53) Habrioux, A.; Sibert, E.; Servat, K.; Vogel, W.; Kokoh, K. B.; Alonso-Vante, N. *J. Phys. Chem. B* **2007**, *111*, 10329−10333.
(54) Habrioux, A.; Vogel, W.; Guinel, M.; Guetaz, L.; Servat, K.; Kokoh, B.; Alonso-Vante, N. *Phys. Chem. Chem. Phys.* **2009**, *11*, 3573−3579.
(55) Kim, H. J.; Kim, D. Y.; Han, H.; Shul, Y. G. *J. Power Sources* **2006**, *159*, 484−490.
(56) Möller, H.; Pistorius, P. C. *J. Electroanal. Chem.* **2004**, *570*, 243−255.
(57) Nakanishi, M.; Takatani, H.; Kobayashi, Y.; Hori, F.; Taniguchi, R.; Iwase, A.; Oshima, R. *Appl. Surf. Sci.* **2005**, *241*, 209−212.
(58) Wang, L.; Yamauchi, Y. *Chem.—Eur. J.* **2011**, *17*, 8810−8815.
(59) Vassilyev, Y. B.; Khazova, O. A.; Nikolaeva, N. N. *J. Electroanal. Chem.* **1985**, *196*, 105−125.
(60) Bae, I. T.; Yeager, E.; Xing, X.; Liu, C. C. *J. Electroanal. Chem.* **1991**, *309*, 131−145.
(61) Beden, B.; Largeaud, F.; Kokoh, K. B.; Lamy, C. *Electrochim. Acta* **1996**, *41*, 701−709.
(62) Park, S.; Chung, T. D.; Kim, H. C. *Anal. Chem.* **2003**, *75*, 3046−3049.
(63) Yuan, J.; Wang, K.; Xia, X. *Adv. Funct. Mater.* **2005**, *15*, 803−809.
(64) Song, Y.; Zhang, D.; Gao, W.; Xia, X. *Chem.—Eur. J.* **2005**, *11*, 2177−2182.
(65) Sakamoto, M.; Takamura, K. *Bioelectrochem. Bioenerg.* **1982**, *9*, 571−582.
(66) Xonoglou, N.; Moumtzis, I.; Kokkinidis, G. *J. Electroanal. Chem.* **1987**, *237*, 93−104.
(67) Wittstock, G.; Strübing, A.; Szargan, R.; Werner, G. *J. Electroanal. Chem.* **1998**, *444*, 61−73.
(68) Zhang, X.; Chan, K. Y.; You, J. K.; Lin, Z. G.; Tseung, A. C. C. *J. Electroanal. Chem.* **1997**, *430*, 147−153.
(69) Kokkinidis, G.; Xonoglou, N. *Bioelectrochem. Bioenerg.* **1985**, *14*, 375−387.

(70) Yeo, I. H.; Johnson, D. C. *J. Electroanal. Chem.* **2001**, *495*, 110–119.
(71) Sun, Y.; Buck, H.; Mallouk, T. E. *Anal. Chem.* **2001**, *73*, 1599–1604.
(72) Yeo, I. H.; Johnson, D. C. *J. Electroanal. Chem.* **2000**, *484*, 157–163.
(73) Wang, J.; Thomas, D. F.; Chen, A. *Anal. Chem.* **2008**, *80*, 997–1004.